

Implementation of DSC model and application for analysis of field pile tests under cyclic loading

Changming Shao^{*†} and Chandra S. Desai[‡]

Department of Civil Engineering and Engineering Mechanics, University of Arizona, P.O. Box 210072, Tucson, AZ 85721-0072, U.S.A.

SUMMARY

The disturbed state concept (DSC) model, and a new and simplified procedure for unloading and reloading behavior are implemented in a nonlinear finite element procedure for dynamic analysis for coupled response of saturated porous materials. The DSC model is used to characterize the cyclic behavior of saturated clays and clay–steel interfaces. In the DSC, the relative intact (RI) behavior is characterized by using the hierarchical single surface (HISS) plasticity model; and the fully adjusted (FA) behavior is modeled by using the critical state concept. The DSC model is validated with respect to laboratory triaxial tests for clay and shear tests for clay–steel interfaces. The computer procedure is used to predict field behavior of an instrumented pile subjected to cyclic loading. The predictions provide very good correlation with the field data. They also yield improved results compared to those from a HISS model with anisotropic hardening, partly because the DSC model allows for degradation or softening and interface response. Copyright © 2000 John Wiley & Sons, Ltd.

KEY WORDS: constitutive model; disturbed state concept; finite element method; soil–structure interaction; cyclic loading; field validation

INTRODUCTION

Geotechnical and structural problems can be complex and there are often no analytical solutions available. Numerical approximation is then an easy and practical way to solve the problems. Among available numerical methods, the finite element method is very popular and can be used for complex situations. An appropriate constitutive law is essential for realistic predictions of the behavior of geotechnical structures using numerical methods. Many models are now available for predicting the behaviour of soils, such as the disturbed state concept (DSC) model which has been recently developed and applied to a wide range of materials [1–5].

In this paper, the DSC model is implemented in a two-phase finite element procedure. A field pile test [6] conducted at Sabine, Texas is simulated by using the finite element program which

^{*} Correspondence to: C. Shao, Department of Civil Engineering and Engineering Mechanics, University of Arizona, P.O. Box 210072 Tucson, AZ 85721-0072, U.S.A.

[†]Research Associate

[‡]Regents' Professor

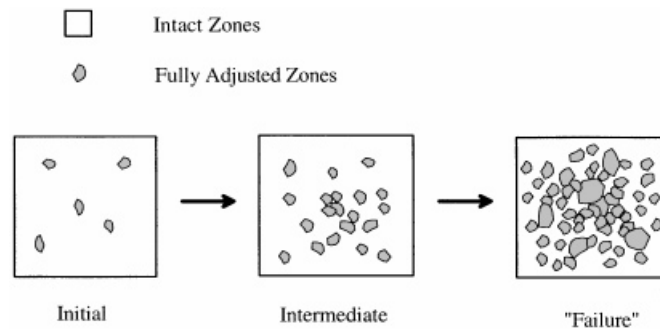


Figure 1. Schematic of growth of the fully adjusted state (FAS).

incorporates the DSC model. Results are compared with those from the field tests. The simulated test sequences include (a) consolidation after the pile was driven into the soil, (b) a tension test (one way loading test) at the end of consolidation and (c) a two-way cyclic load test. New unloading and reloading modelling schemes are proposed in the study; they are simple yet give realistic prediction of unloading and reloading behaviour of the geomaterials under cyclic loading. The scope of the paper includes

- (a) description of the DSC model,
- (b) implementation of the DSC model in the finite element program, and
- (c) validation of the model against the field tests for the instrumented pile.

DISTURBED STATE CONCEPTS

The disturbed state concept (DSC) has been developed recently as a unified constitutive modelling approach. It has been successfully verified with respect to test data for interfaces [2], cohesionless soils [3], undrained clay [4] and saturated clay–steel interfaces [5].

The original idea for the DSC was proposed by Desai [7], and subsequently formalized for various applications. In the DSC, the material is assumed to transform continuously and randomly from the relatively intact (RI) state to the fully adjusted (FA) state (see Figure 1) under external excitation such as mechanical or thermal forces. The transformation involves micro-structural changes that cause particle reorientation and relative motions. The fully adjusted (FA) state is an asymptotic state that can not be further disturbed. The observed response of the material is expressed in terms of the responses of RI state which excludes the effects of disturbance, and that of FA state which is often assumed to be the critical state. The transformation of material from RI state to FA state is defined by the disturbance function D .

Reference state I: relative intact state

The relative intact (RI) state is an idealized state which excludes the disturbance effects. Elastic, elasto-plastic or visco-plastic models can be used to characterize the RI state. Here the basic model in the HISS family, δ_0 model [8], is used to represent the behaviour of material in the RI state. The δ_0 model is based on associative plasticity and isotropic hardening. The yield function

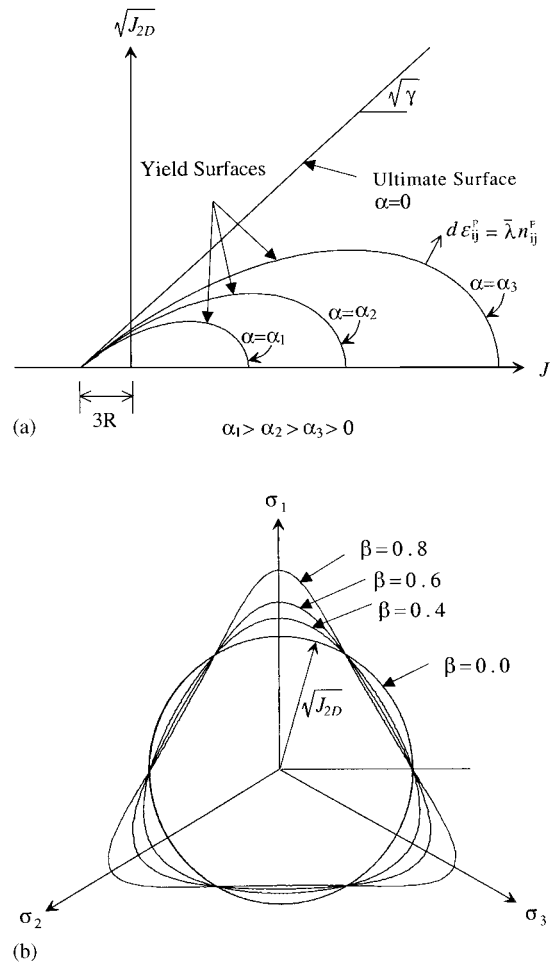


Figure 2. Yield surfaces of HISS model: (a) yield surfaces in $J_1 - \sqrt{J_{2D}}$ plane, and (b) yield surfaces in the octahedral plane.

in the δ_0 model is given as [8,9]

$$F = \frac{J_{2D}}{p_a^2} - \left(-\alpha \left(\frac{J_1^*}{p_a} \right)^n + \gamma \left(\frac{J_1^*}{p_a} \right)^2 \right) (1 - \beta S_r)^{-0.5} = 0 \quad (1)$$

where stress ratio $S_r = \sqrt{27/2} J_{3D}/J_{2D}^{1.5}$; $J_1^* = J_1 + 3R$; J_1 is the first invariant of stress tensor σ_{ij} ; J_{2D} and J_{3D} are the second and third invariants of the deviatoric stress tensor S_{ij} ; p_a is the atmospheric pressure; γ , β , n and R are material parameters; and α is the hardening function. Figure 2(a) shows the shape of the yield surface in the $J_1 - \sqrt{J_{2D}}$ space ($S_r = \text{constant}$), and Figure 2(b) the shape of the yield surface in the octahedral space ($J_1 = \text{constant}$).

The form of hardening function α used here is given by

$$\alpha = \frac{h_1}{(\xi_v + h_3 \xi_D^{h_4})^{h_2}} \quad (2)$$

where h_1, h_2, h_3 and h_4 are material parameters, ξ is the trajectory of the plastic strain ε_{ij}^p , ξ_v is the volumetric part of the plastic strain defined as

$$d\xi_v = \begin{cases} \frac{1}{\sqrt{3}} d\varepsilon_{ii}^p & \text{if } d\varepsilon_{ii}^p > 0 \text{ (compression)} \\ 0 & \text{if } d\varepsilon_{ii}^p < 0 \text{ (dilation)} \end{cases} \quad (3)$$

while ξ_D is the trajectory of the deviatoric plastic strain defined as

$$d\xi_D = \sqrt{dE_{ij}^p dE_{ij}^p} \quad (4)$$

where E_{ij}^p is the tensor of deviatoric plastic strain $\varepsilon_{ij}^p - \frac{1}{3}\delta_{ij}\varepsilon_{kk}^p$.

According to the plasticity theory, the incremental stress-strain equation can be derived as

$$d\sigma_{ij} = C_{ijkl}^{ep} d\varepsilon_{kl} \quad (5)$$

where

$$C_{ijkl}^{ep} = C_{ijkl}^e - \frac{C_{ijrs}^e n_{rs}^Q (\partial F / \partial \sigma_{pq}) C_{pqkl}^e}{(\partial F / \partial \sigma_{mn}) C_{mnpq}^e n_{pq}^Q - \partial F / \partial \xi} \quad (6)$$

where C_{ijkl}^e is the elastic constitutive tensor, and n_{ij}^Q is the tensor defining the direction of plastic deformation as

$$n_{ij}^Q = \frac{\partial F / \partial \sigma_{ij}}{((\partial F / \partial \sigma_{kl}) (\partial F / \partial \sigma_{kl}))^{1/2}} = \frac{\partial F / \partial \sigma_{ij}}{\|\partial F / \partial \sigma_{kl}\|} \quad (7)$$

Reference state II: fully adjusted state

The critical state concept [1,10] is used here to characterize the FA material (Figure 3). For soils, the critical void ratio e^c the material attains in a shear test is related to hydrostatic stress J_1^c at the critical state as

$$e^c = e^{oc} - \lambda \ln \left(\frac{J_1^c}{3p_a} \right) \quad (8)$$

where e^{oc} is the critical void ratio when $J_1^c = 3p_a$; λ is a material constant and superscript 'c' denotes the quantities at the critical state. At the critical state, the maximum shear stress the material can carry is given by

$$\sqrt{J_{2D}^c} = \bar{m} J_1^c \quad (9)$$

where \bar{m} is a material parameter, and $\sqrt{J_{2D}^c}$ is the value of $\sqrt{J_{2D}}$ at the critical state.

Disturbance function

At the beginning of loading, D is zero (or a small value depending on the initial condition). As the load increases the deformation increases and disturbance increases. When D approaches 1, the material approaches the ultimate (critical) state. The following function is used here to represent

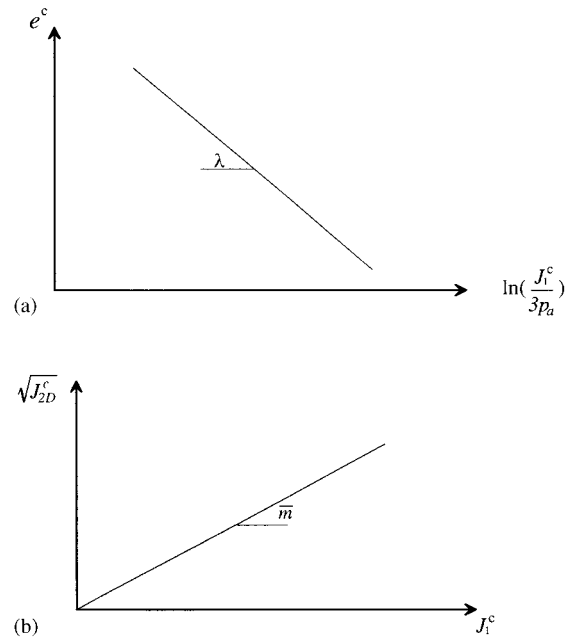


Figure 3. Relations in critical state: (a) in $e^c - \ln(J_1^c/3p_a)$ space, and (b) in $J_1^c - \sqrt{J_{2D}^c}$ space.

the disturbance:

$$D = D_u(1 - \exp(-A\epsilon_{2D}^Z)) \quad (10)$$

where A , Z , and D_u ($< = 1$) are material parameters.

Constitutive equations

The incremental form of the stress relation can be found as [1, 4]

$$d\sigma_{ij}^a = (1 - D)d\sigma_{ij}^i + Dd\sigma_{ij}^c + dD(\sigma_{ij}^c - \sigma_{ij}^i) \quad (11)$$

where the superscripts 'a', 'i' and 'c' denote the observed (average) stress and stresses in the RI and FA states, respectively. The final incremental form is derived as [11]

$$d\sigma_{ij}^a = C_{ijkl}^{DSC} d\epsilon_{kl} \quad (12)$$

where

$$C_{ijkl}^{DSC} = (1 - D)C_{ijkl}^{ep} + DM_{ij}\delta_{kl} + DN_{ijkl} + (\sigma_{ij}^c - \sigma_{ij}^i)R_{kl} \quad (13)$$

$$M_{ij} = \frac{J_1^c}{\lambda}(1 + e_0) \left(\frac{\bar{m}S_{ij}^i}{\sqrt{J_{2D}^i}} + \frac{1}{3}\delta_{ij} \right) \quad (14)$$

$$N_{ijkl} = \frac{J_1^c \bar{m}}{\sqrt{J_{2D}^i}} \left[\left(C_{ijkl}^{ep} - \frac{1}{3} \delta_{ij} C_{mmkl}^{ep} \right) - \frac{S_{ij}^i S_{mn}^i}{2J_{2D}^i} C_{mnkl}^{ep} \right] \quad (15)$$

$$R_{kl} = D_u A e^{-A \xi_D^Z} Z \xi_D^{Z-1} \left(n_{pq}^o n_{pq}^o - \frac{1}{3} n_{pp}^o n_{qq}^o \right)^{1/2} \frac{(\partial F / \partial \sigma_{ij}) C_{ijkl}^e}{\partial F / \partial \sigma_{mn} C_{mnst}^e n_{st}^o - \partial F / \partial \xi} \quad (16)$$

Details of the derivation are given by Shao [11].

Stress-strain relations for unloading and reloading

Geomaterials show non-linear behaviour during non-virgin loading (unloading and reloading) (Figure 4). In the classical plasticity theory, the non-virgin loading is assumed to be linear elastic; such models may give satisfactory results for the problems involving few stress reversals (unloading/reloading). For problems with cyclic loading, the errors during non-virgin loading for each cycle can accumulate and the final results may not be acceptable. To account for the non-linearity during non-virgin loading, extensions of the plasticity theory are proposed. Two popular approaches are (a) defining the non-virgin plastic modulus as a function of virgin plastic modulus at some reference points on the prestress surface (the yield surface before unloading) and the distance from the current stress point to the prestress surface [9,12], and (b) nested surface models [13–15].

One of the new contributions in this paper is a simplified approach for the unloading and reloading behaviour. It provides satisfactory simulation of unloading and reloading without the need for complex motion of yield surfaces, and hence, is computationally efficient and economical.

Unloading interpolation function

During unloading, the following interpolation function is proposed:

$$d\sigma_{ij} = C_{ijkl}^{UL} d\varepsilon_{kl} \quad (17)$$

where C_{ijkl}^{UL} is a constitutive tensor the same as the elastic constitutive tensor except that in Equation (17), Young's modulus E is a variable— E^u (ν is kept constant) (Figure 4(a)). Equation (17) can be specialized for the stress path of conventional triaxial compression (CTC) tests as

$$d\sigma_1 = E^u d\varepsilon_1 \quad (18)$$

The unloading modulus E^u can be evaluated as

$$\frac{1}{E^u} = \frac{1}{E^{BUL}} + \frac{1}{E^p} \quad (19)$$

where E^{BUL} is the slope of the unloading curve at the beginning of the unloading (point A in Figure 4(a)), for which Young's modulus of the material can be used; and E^p is the modulus which causes the inelastic ('plastic') strain. E^p is evaluated by using the following function:

$$E^p = p_a K_1 \left(\frac{p_a}{\sqrt{J_{2D}^0}} - \sqrt{J_{2D}} \right)^{K_2} \quad (20)$$

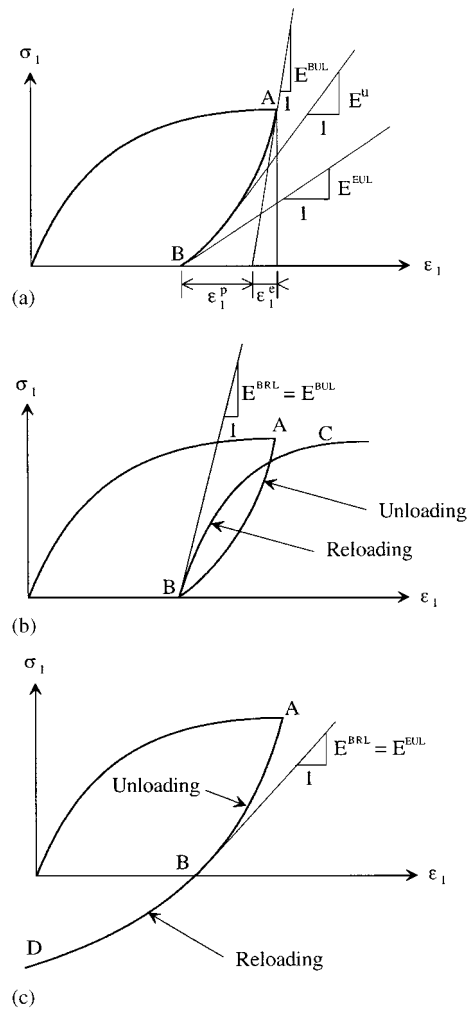


Figure 4. Unloading and reloading curves in CTC tests: (a) unloading, (b) reloading case 1 and (c) reloading case 2.

where K_1 and K_2 are (internal) constants; p_a is the atmospheric pressure used here to non-dimensionalize K_1 and K_2 ; J_{2D}^0 and J_{2D} are the second invariants of deviatoric stress tensors at the beginning of unloading (point A) and at the current state during the unloading, respectively. For example, for the CTC test ($\sigma_1 > \sigma_2 = \sigma_3$):

$$\sqrt{J_{2D}} = \frac{\sigma_1 - \sigma_3}{\sqrt{3}} \quad (21)$$

$$E^p = p_a K_1 \left(\frac{\sqrt{3} p_a}{\sigma_1^0 - \sigma_1} \right)^{K_2} \quad (22)$$

where σ_1^0 is the axial stress at the beginning of unloading and σ_1 is the current axial stress during the unloading.

From equations (18) and (19), the incremental strain during unloading can be expressed as

$$d\varepsilon_1 = \frac{d\sigma_1}{E^u} = \frac{d\sigma_1}{E^{\text{BUL}}} + \frac{d\sigma_1}{E^p} = d\varepsilon_1^e + d\varepsilon_1^p \quad (23)$$

where $d\varepsilon_1^e$ is the elastic strain and $d\varepsilon_1^p (= d\sigma_1/E^p)$ is the 'plastic' strain (Figure 4(a)). At the beginning of the unloading, Equation (22) leads to $E^p = \infty$ thus $d\varepsilon_1^p = 0$. This ensures the initial elastic unloading.

Determination of unloading parameters

As shown in Figure 4(a), three parameters, E^{BUL} , E^{EUL} and ε_1^p , can be easily obtained from the CTC tests: E^{BUL} = slope of the stress-strain curve at the beginning of unloading. Young's modulus of the material, E , can be used if E is determined as the initial unloading slope, E^{EUL} = slope of the stress strain curve at the end of unloading, and ε_1^p = plastic strain accumulated during unloading.

At the end of the unloading, $\sigma_1 = \sigma_1^{\text{EUL}} = \sigma_3$, then

$$\frac{1}{E^u} = \frac{1}{E^{\text{BUL}}} + \frac{1}{K_1 p_a} \left(\frac{\sigma_1^0 - \sigma_1^{\text{EUL}}}{\sqrt{3} p_a} \right)^{K_2} = \frac{1}{E^{\text{EUL}}} \quad (24)$$

and

$$\begin{aligned} \varepsilon_1^p &= \int d\varepsilon_1^p = \int \frac{d\sigma_1}{E^p} = \int_{\sigma_1^{\text{EUL}}}^{\sigma_1^0} \frac{1}{K_1 p_a} \left(\frac{\sigma_1^0 - \sigma_1}{\sqrt{3} p_a} \right)^{K_2} d\sigma_1 \\ &= \frac{\sqrt{3}}{K_1 (K_2 + 1)} \left(\frac{\sigma_1^0 - \sigma_1^{\text{EUL}}}{\sqrt{3} p_a} \right)^{K_2 + 1} \end{aligned} \quad (25)$$

Solving equations (24) and (25) yields

$$K_2 = \frac{\sigma_1^0 - \sigma_1^{\text{EUL}}}{\varepsilon_1^p} \left(\frac{1}{E^{\text{EUL}}} - \frac{1}{E^{\text{BUL}}} \right) - 1 \quad (26)$$

$$K_1 = \frac{\sqrt{3}}{(K_2 + 1) \varepsilon_1^p} \left(\frac{\sigma_1^0 - \sigma_1^{\text{EUL}}}{\sqrt{3} p_a} \right)^{K_2 + 1} \quad (27)$$

For other stress paths, similar equations can be derived [11]. For simplicity, the foregoing parameters are assumed constant for all cycles. However, σ_1^0 , σ_1^{EUL} , E^{BUL} , E^{EUL} and ε_1^p may depend on number of cycles, disturbance or plastic strain. Thus, in general, K_1 and K_2 can be functions of disturbance or plastic strain.

Reloading function

The following interpolation function is proposed for reloading (Figures 4(b) and 4(c)):

$$d\sigma_{ij}^a = R C_{ijkl}^{\text{DSC}} d\varepsilon_{kl} + (1 - R) C_{ijkl}^c d\varepsilon_{kl} \quad (28)$$

where R is the interpolation variable to be so defined such that $R = 0$ at the beginning of reloading and $R = 1$ at the end of reloading. So at the beginning of reloading, the loading is elastic and at the end of the reloading, it becomes virgin loading.

In this research, R is defined as $R = \sqrt{J_{2D}}/\sqrt{J_{2D}^0}$, where J_{2D}^0 is the second invariant of the deviatoric stress tensor at the beginning of the last unloading, and J_{2D} the second invariant of the current deviatoric stress tensor.

There are two cases of reloading, Figure 4(b) and 4(c). Young's modulus used in C_{ijkl}^{DSC} and C_{ijkl}^e for reloading E^R , is different in the two cases. Young's modulus at the beginning of reloading, $E^{BRL} = E^{BUL}$ (unloading slope at the beginning of the unloading) for case 1, Figure 4(b) and $E^{BRL} = E^{EUL}$ (unloading slope at the end of the unloading) for case 2 (Figure 4(c)).

In the finite element analysis, the reloading stress path may be somewhere in between the two cases. So a number S is defined as an indication of the direction of reloading:

$$S = \frac{(\sigma_{ij}^0 - \sigma_{ij}) d\sigma_{ij}}{\|\sigma_{ij}^0 - \sigma_{ij}\| \|d\sigma_{ij}\|}, \quad -1 \leq S \leq 1 \quad (29)$$

where σ_{ij}^0 , σ_{ij} and $d\sigma_{ij}$ are the stress tensor before unloading, the current stress and next stress increment, respectively. $S = -1$ indicates case 1 reloading and $S = 1$ indicates case 2 loading. E^{BRL} is interpolated between E^{BUL} and E^{EUL} as

$$\frac{1}{E^{BRL}} = \frac{1-S}{2E^{BUL}} + \frac{1+S}{2E^{EUL}} \quad (30)$$

During the reloading, E^R is interpolated as

$$\frac{1}{E^R} = \frac{1-R}{E^{BRL}} + \frac{R}{E} \quad (31)$$

where E is Young's modulus of the material. Thus at the beginning of reloading ($R = 0$), $E^R = E^{BRL}$, which ensures the smooth transition from unloading to reloading in case 2. At the end of reloading $E^R = E$, which ensures the smooth transition from reloading to virgin loading.

Laboratory tests and parameters of soils and interfaces

Laboratory tests on the Sabine Clay [4] and the steel–clay interface [5] are used to find the parameters and verify the models. Specimens of undisturbed Sabine Clay were obtained from the pile test site at Sabine Pass, Texas, and tested under triaxial and multiaxial loading with various confining stresses and stress paths [4]. For the interface tests, three types of tests were conducted on the remolded Sabine Pass clays and the clay–steel interfaces, namely consolidation tests, simple shear tests and direct shear tests [5].

The procedure of parameter determination for the DSC and HISS models by using tests with different stress paths can be found in References [11,16]. The parameters for the proposed unloading procedures are found from the unloading curve. Though the interface tests are used to find the parameters, the DSC model used in this research is based on a 'solid' thin-layer interface model [17]. The parameters from the interface tests are transformed for the solid element [11]. Material parameters found are listed in Table I.

Table I. Material parameters used for finite element analyses.

	Clay	Interface
Relative intact state:		
E	10 350 kPa	4300 kPa
ν	0.35	0.42
γ	0.047	0.077
β	0	0
m	- 0.5	- 0.5
n	2.8	2.6
$3R$	0	0
h_1	0.0001	0.000408
h_2	0.78	2.95
h_3	0	0.0203
h_4	0	0.0767
Critical state:		
λ	0.1692	0.298
e^{oc}	0.9033	1.359
\bar{m}	0.0694	0.123
Disturbance function:		
D_u	0.75	1
A	1.73	0.816
Z	0.3092	0.418
Unloading and reloading:		
E^{BUL}	34500 kPa	4300 kPa
E^{EUL}	3450 kPa	400 kPa
ε_1^p	0.005	0.0305
Other parameters:		
Permeability, k	2.39×10^{-10} m/s	2.39×10^{-10} m/s
Density of soils, ρ_s	2.65 Mg/m ³	2.65 Mg/m ³
Bulk modulus of soil grain, K_s	10^9 kPa	10^9 kPa
Bulk modulus of water, K_f	10^8 kPa	10^8 kPa
Density of water, ρ_f	1.0 Mg/m ³	1.0 Mg/m ³

Validation of DSC model

The DSC model is validated with respect to laboratory tests on the soil and interfaces. Typical results are included here.

The triaxial test of the clay with a confining stress $\sigma_2 = 276$ kPa is simulated by using the finite element program with 16 four-node elements (Figure 5). One quarter of the specimen is used in the simulation due to symmetry of the problem. The predicted stress and pore water pressure are shown in Figures 6(a) and 6(b). It can be seen that the procedure predicted the peak values of the stresses very well. However, the predicted stress reaches its peak at lower strain than that in the laboratory test. The predicted pore pressures are close to those from the test.

The interface test under normal stress $\sigma_n = 138$ kPa is back predicted using the mesh shown in Figure 7. Figure 8 shows the shear stresses in the interface from both the test and finite element predictions for the cycles 1, 2, 3, 4, 5, 10, 25, 50 and 100. It can be seen that the shear stresses from the finite element predictions (Figure 8(b)) agree well with those from the test (Figure 8(a)). The peak value of the shear stress in the first cycle from the finite element analysis is very close to that

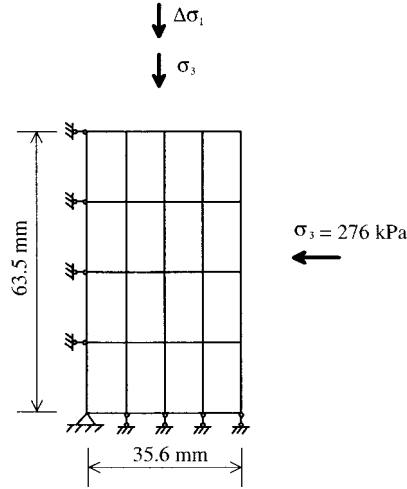


Figure 5. Finite element mesh for the triaxial specimen.

from the test. The predicted pore pressures (Figure 9(b)) are lower than those in the test (Figure 9(a)) at higher cycles. But the trend of pore water pressure development agrees with that in the test.

FINITE ELEMENT PROCEDURE

Soils and rocks are porous materials consisting of skeleton (formed by individual particles) and voids. When the voids are filled with water or any other fluid, the soil becomes a two-phase system and its behaviour is coupled. Under external excitation, the skeleton deforms partly due to deformation of individual particles and partly due to relative motions between particles. On the other hand, the pressure in the fluid changes and the fluid flows from places with high excess pore pressure to where the excess pore pressure is low.

Constitutive equations for elastic porous material were first derived by Biot [18] and later extended to non-linear system in incremental form by Zienkiewicz [19]. The finite element equations for the coupled problem are derived as [11,20]

$$\begin{bmatrix} M_{uuij}^{ac} & M_{uwi j}^{ad} \\ M_{wuij}^{bc} & M_{wwij}^{bd} \end{bmatrix} \begin{Bmatrix} \dot{U}_j^c \\ \dot{W}_j^d \end{Bmatrix} + \begin{bmatrix} 0 & 0 \\ 0 & C_{wwij}^{bd} \end{bmatrix} \begin{Bmatrix} \dot{U}_j^c \\ \dot{W}_j^d \end{Bmatrix} + \begin{Bmatrix} \int_V N_{u,j}^a \sigma_{ij} dV \\ \int_V N_{w,i}^b p dV \end{Bmatrix} = \begin{Bmatrix} f_{ui}^a \\ f_{wi}^b \end{Bmatrix} \quad (32)$$

where a, b are indices to the nodes, c, d are summation indices for the nodes in the whole domain, and indices i, j are for the degrees of the freedom at each node. M_{uuij}^{ac} , $M_{uwi j}^{ad}$, M_{wuij}^{bc} and M_{wwij}^{bd} are the mass matrices; C_{wwij}^{bd} is the damping matrix; N_u^a , N_w^b are the shape functions for the solid and fluid phases; and f_{ui}^a and f_{wi}^b are the overall load and the load on the fluid.

In a simple form, Equation (32) may be written as

$$[M]\{\ddot{x}\} + [C]\{\dot{x}\} + [K]\{x\} = \{Q\} \quad (33)$$

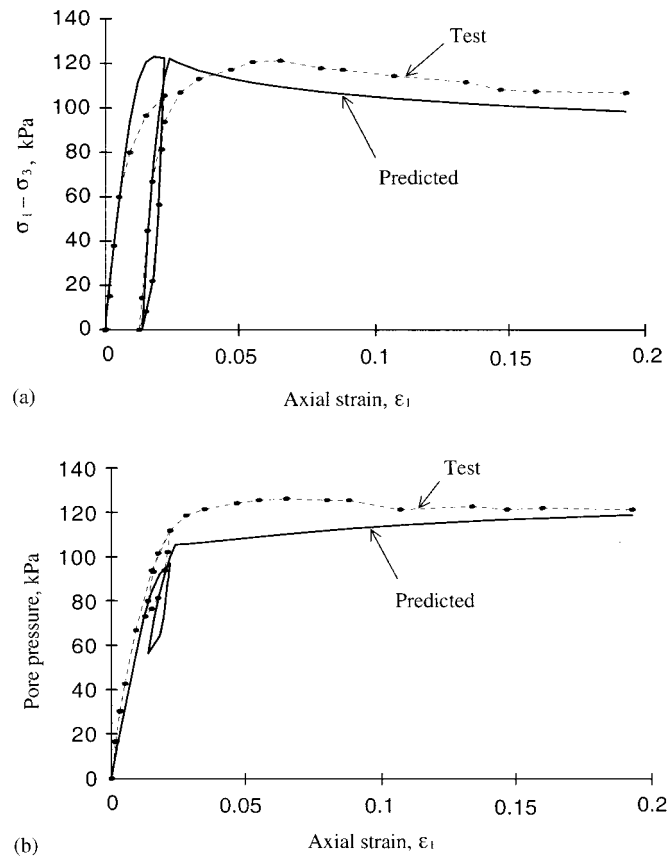


Figure 6. Comparison of predicted and observed behaviour CTC test, confining stress = 276 kPa (40 psi). $e_0 = 0.8614$: (a) axial stress vs axial strain and (b) pore pressure vs axial strain.

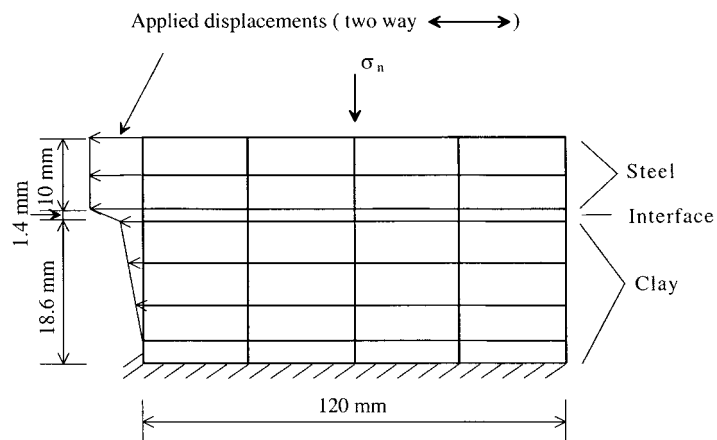


Figure 7. Finite element mesh for the interface.

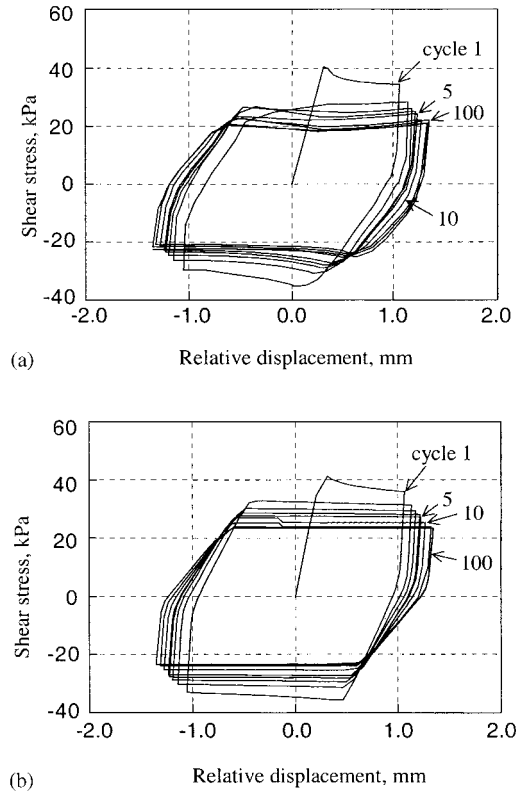


Figure 8. Comparison of shear stresses from test and FEM (normal stress = 138 kPa, Cycles 1, 2, 3, 4, 5, 10, 25, 50 and 100): (a) test and (b) FEM prediction.

where $[M]$, $[C]$ and $[K]$ represent the mass, damping and stiffness matrices of the system, respectively; $\{Q\}$ represents the loads on the system; $\{x\}$, $\{\dot{x}\}$ and $\{\ddot{x}\}$ are displacements, velocities and accelerations at each degree of freedom.

The family of Newmark's methods of time integration is used in this study, in which the values of $\{x\}$, $\{\dot{x}\}$ and $\{\ddot{x}\}$ at time t_{n+1} can be found when their values at time t_n are known:

$$[K^*]\{x(t_{n+1})\} = \{Q^*\} \quad (34)$$

where

$$[K^*] = \frac{1}{\beta \Delta t^2} [M] + \frac{\gamma}{\beta \Delta t} [C] + [K] \quad (35)$$

$$\begin{aligned} \{Q^*\} = \{Q(t_{n+1})\} + [M] & \left\{ \frac{x(t_n)}{\beta \Delta t^2} + \frac{\dot{x}(t_n)}{\beta \Delta t} + \left(\frac{1}{2\beta} - 1 \right) \ddot{x}(t_n) \right\} \\ & + [C] \left\{ \frac{\gamma}{\beta \Delta t} x(t_n) + \left(\frac{\gamma}{\beta} - 1 \right) \dot{x}(t_n) + \left(\frac{\gamma}{2\beta} - 1 \right) \Delta t \ddot{x}(t_n) \right\} \end{aligned} \quad (36)$$

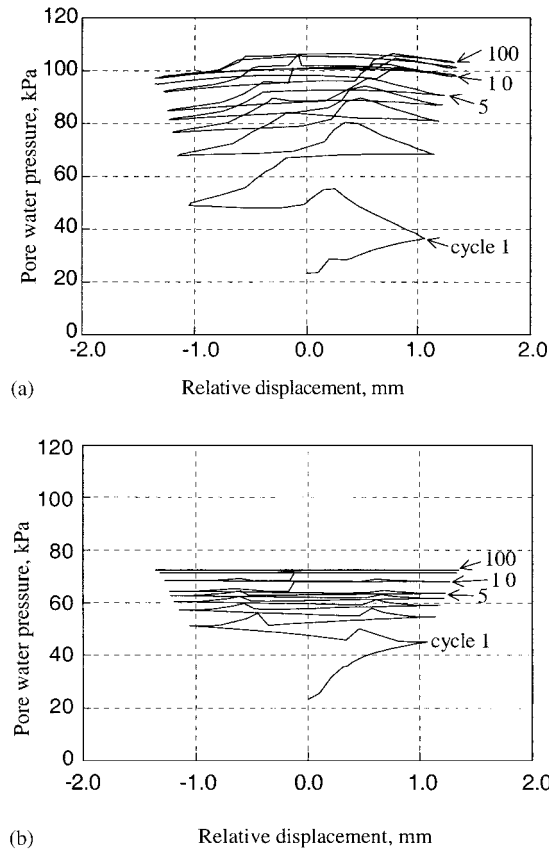


Figure 9. Comparison of pore water pressures from test and FEM (normal stress = 138 kPa, cycles 1, 2, 3, 4, 5, 10, 25, 50 and 100): (a) test and (b) FEM prediction.

$$\{\ddot{x}(t_{n+1})\} = \frac{1}{\beta \Delta t^2} \{x(t_{n+1}) - x(t_n) - \Delta t \dot{x}(t_n)\} - \frac{1-2\beta}{2\beta} \{\ddot{x}(t_n)\} \quad (37)$$

$$\{\dot{x}(t_{n+1})\} = \{\dot{x}(t_n)\} + \Delta t \{(1-\gamma)\ddot{x}(t_n) + \gamma\ddot{x}(t_{n+1})\} \quad (38)$$

where $\Delta t = t_{n+1} - t_n$, γ and β are parameters in the Newmark's scheme.

For the non-linear system, iterations need to be employed to find $\{x(t_{n+1})\}$. At iteration r , the equation for the next increment, $\{dx^r\}$, can be expressed as

$$[K^*]\{dx^r(t_{n+1})\} = \{F_{n+1}^*\} \quad (39)$$

where

$$\{F_{n+1}^*\} = \{Q_{n+1}^*\} - [K^*]\{x^r(t_{n+1})\} \quad (40)$$

The Newmark's scheme for linear systems has been found to be unconditionally stable if $2\beta \geq \gamma \geq 0.5$.

Computational algorithms

An incremental procedure combined with the general Newton–Raphson scheme is adopted here. The steps in the algorithm are given below:

- (1) Initialization: Known or assumed initial conditions.

$$\{\sigma^i\} = \{\sigma^a\} = \{\sigma_0^a\}, \quad D = 0 \quad (41)$$

For hardening function, assume the initial stress is on the yield surface. Then

$$\alpha_0 = \left(\gamma - \frac{J_{2D}^i}{(J_1^i)^2 (1 - \beta S_r)^m} \right) \left(\frac{J_1^i}{p_a} \right)^{2-n} \quad (42)$$

$$\xi_D = 0 \quad \text{and} \quad \xi_V = \left(\frac{h_1}{\alpha_0} \right)^{1/h_2} \quad (43)$$

Here the subscript ‘0’ denotes initial conditions.

- (2) Set load/time increment number $n = 0$.
 (3) Set iteration number $r = 0$.
 (4) Calculate the unbalanced load for this load step:

$$\{F_{n+1}\}^{(r)} = \{Q_{n+1}\} - \int_V [B]^T \{\sigma_n^a\}^{(r)} dV \quad (44)$$

For dynamic or consolidation problems, $\{F_{n+1}\}$ is modified according to Equation (40).

- (5) Calculate stiffness:

$$[K_n]^{(r)} = \int_V [B]^T [C^{DSC}]^{(r)} [B] dV \quad (45)$$

For dynamic or consolidation problems, $[K_n]$ is modified according to Equation (35).

- (6) Calculate incremental displacements:

$$\{dq\}^{(r)} = [K_n]^{(r-1)} \{F_{n+1}\}^{(r)} \quad (46)$$

- (7) Calculate incremental strains:

$$\{d\epsilon^a\}^{(r)} = [B] \{dq\}^{(r)} \quad (47)$$

- (8) Calculate stresses in the relative intact part and in the fully adjusted part:

$$\{d\sigma^i\}^{(r)} = [C^{ep}] \{d\epsilon\}^{(r)} \quad (48)$$

$$\{\sigma^i\}^{(r+1)} = \{\sigma^i\}^{(r)} + \{d\sigma^i\}^{(r)} \quad (49)$$

Drift correction (see below) is performed here on $\{\sigma^i\}$ so as to stay on or inside the yield surface. Stresses in the FA state are calculated as

$$J_1^c = 3p_a \exp\left(\frac{e^{oc} - e^c}{\lambda}\right) \quad (50)$$

$$\sqrt{J_{2D}^c} = \bar{m} J_1^c \quad (51)$$

$$\{\sigma^c\}^{(r+1)} = \frac{1}{3} J_1^c \{\delta\} + \frac{\sqrt{J_{2D}^c}}{\sqrt{J_{2D}^i}} \left\{ \{\sigma^i\}^{(r+1)} - \frac{1}{3} J_1^i \{\delta\} \right\} \quad (52)$$

(9) Update D , $\{\sigma^a\}$:

$$d\zeta_D = \sqrt{\{dE^{p(i)}\}^T \{dE^{p(i)}\}} \quad (53a)$$

$$\zeta_D^{(r+1)} = \zeta_D^{(r)} + d\zeta_D \quad (53b)$$

$$D = D_u(1 - e^{-A\zeta_D^{(r)}}) \quad (54)$$

$$\{\sigma^a\}^{(r+1)} = (1 - D)\{\sigma^i\}^{(r+1)} + D\{\sigma^c\}^{(r+1)} \quad (55)$$

(10) Check convergence.

If $\frac{\|dq_{n+1}^r\|}{\|dq_{n+1}^0\|} < \varepsilon = 10^{-2}-10^{-4}$, convergence is achieved at this load step, go to step 12.

(11) Set $r = r + 1$. If $r < r_{\max}$, go to step 4.

(12) Set $n = n + 1$. If $n < n_{\max}$, go to step 3.

(13) Stop.

Drift correction for virgin loading of the RI part

After an increment of strain for each element is calculated from the displacements, the stress increments are calculated from the constitutive relation, Equation (5), and α is updated from Equation (2). The new stresses will likely be found outside the yield surface ($F > 0$) and need to be corrected to stay on or in the yield surface ($F \leq 0$). The procedure is called drift correction. The modified drift correction method of Potts and Gens [16,21] is used here for the stress in RI part of the material.

ANALYSIS OF PILE LOAD TESTS

The Earth Technology Corporation performed six field tests at Sabine, Texas with the instrumented pile segments of diameter 4.37 cm (1.72 in) and 7.62 cm (3 in). Three tests, full displacement 7.62-cm (3 in), X-probe, and partial displacement 7.62-cm (3 in) piles, were under a joint NSF project with the University of Arizona. Detailed description of pile load tests are given by The Earth Technology Corporation [6]. Typical simulation involving the 7.62-cm (3 in) pile is presented here.

When a pile is driven in a saturated clay mass, the pore pressure around the pile increases and, therefore, reduces the effective stresses around the pile. With the excess pore pressure dissipating with time, the clay is consolidated and becomes stronger. Tension tests to failure at different consolidation levels were carried out to investigate the increase of pile capacity during consolidation. One- and two-way cyclic load tests were carried out near the end of consolidation. In the cyclic load tests, after the shear transfer reached failure, the pile was unloaded until the shear transfer reduced to zero, and then reloaded.

The displacement-controlled tests for the 7.62 cm (3-in) pile probe were numerically simulated using the finite element program with the DSC model. Since shear deformations in saturated clay are almost volume conserved, 'shear locking' was observed when eight node elements with four Gauss integration points were used. Therefore, four node elements with one Gauss integration point were used for both solid and fluid in all the finite element analyses here.

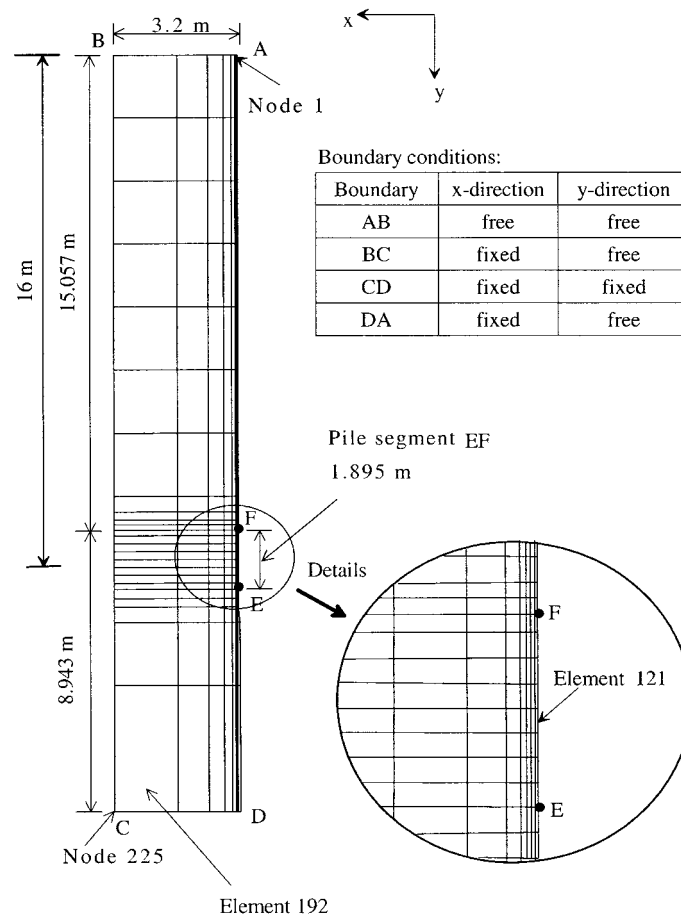


Figure 10. Finite element mesh of field pile test.

The initial stress condition is first established (see below). Then various test sequences are simulated: (a) consolidation, (b) one-way loading test, and (c) two-way cyclic loading test. For each stage, the results of the previous stage are used as the initial conditions.

The mesh used for the simulation, Figure 10, is the same as that used in the previous HISS (δ_0) analysis [16], except that the thin-layer elements are used for the pile–clay interface while in the previous analysis, there were no interface elements. Also, the previous anisotropic hardening model (HISS) did not include effect of disturbance leading to softening or degradation. There are totally 192 elements and 225 nodes. The inner elements in contact with the pile are considered as interface elements with a thickness $t = 1.4$ mm as in the interface tests [5]. The parameters from the interface tests are used for those elements. The rest are clay elements whose material parameters are from laboratory tests on the clay (Table I). The pile is assumed to be rigid, so the pile movements are simulated as prescribed displacements of nodes in contact with the pile (EF in Figure 10). The displacement boundary conditions are also shown in Figure 10.

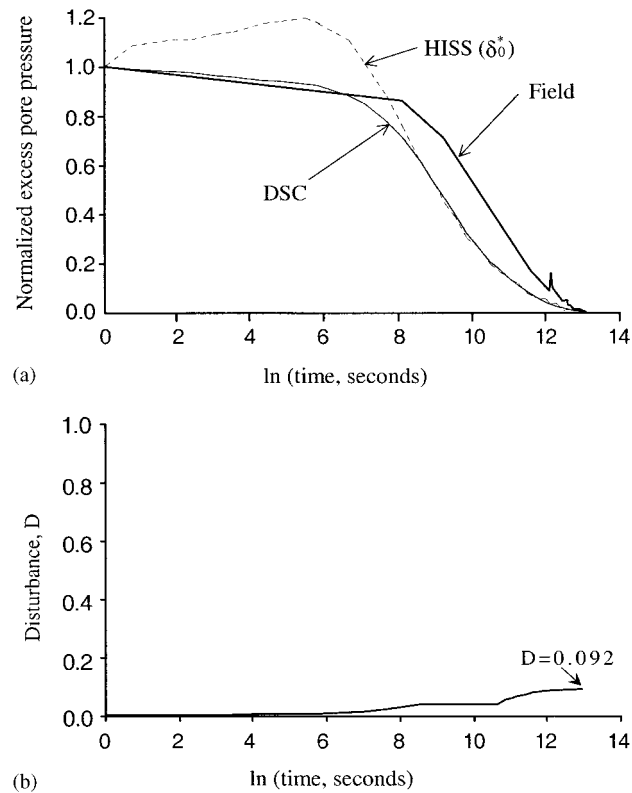


Figure 11. Comparison between field consolidation behaviour and predicted results from HISS and DSC models: (a) normalized excess pore pressure and (b) disturbance.

Driving stresses

Before starting to simulate the process of pile driving, it is necessary to obtain the initial conditions of the soil before pile driving. As in most geotechnical problems, where the water table is at the surface, it is assumed that *in situ* stresses and pore pressures are caused by the weight of soil and fluid and the lateral effective stresses are K_0 times the vertical effective stress. K_0 is the coefficient of earth pressure at rest which is adopted as 0.786 [16]. The initial hardening parameter α_0 is calculated assuming that these stresses are on the yield surface.

When a pile is driven into soil, the soil around and below it gets pushed away to accommodate the pile. The strain path method (SPM), as proposed by Baligh [22,23] is used to simulate the effects of pile driving for pile segments. Strain paths followed by all the Gauss points below the bottom of the borehole during the pile driving process are computed. Once the strain path is known, the stresses can be found by substituting the strains into the constitutive equations. These stresses were adopted from those in the previous analysis of the HISS model [16]. As the deviatoric plastic strains at this stage are small compared to that caused by the later loading, the value of the disturbance is assumed as zero.

Consolidation after pile driving

The consolidation process is simulated until all the excess pore pressure are dissipated. The predicted pore pressure dissipation curves at the center of element 121 (16 m below the ground surface, Figure 10) by the DSC model are compared with field measurements and the prediction from the HISS model by plotting the normalized excess pore pressure with the logarithmic time in Figure 11(a). It can be seen that the normalized dissipation curves correlate well. The DSC gives a much closer correlation with the field results than that from the HISS model [16].

The disturbance developed in element 121 during the consolidation is shown in Figure 11(b). At the end of the consolidation, the disturbance in element 121 is about 0.092.

Simulation of one-way cyclic load test at the end of consolidation

The vertical displacements as in the field are applied to the nodes in contact with pile segment (from E to F in Figure 10) in 134 time steps. The predicted behavior for the test is compared with

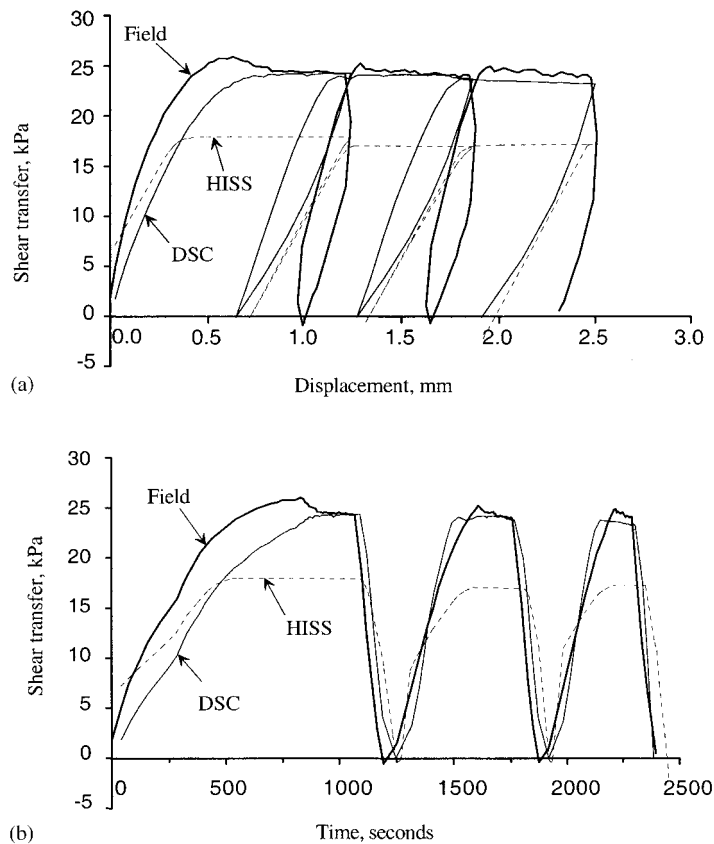


Figure 12. Comparison between field measurements and predictions from DSC and HISS models: one-way cyclic load test: (a) shear transfer vs displacement, (b) shear transfer vs time, (c) pore pressure vs displacement and (d) disturbance vs displacement.

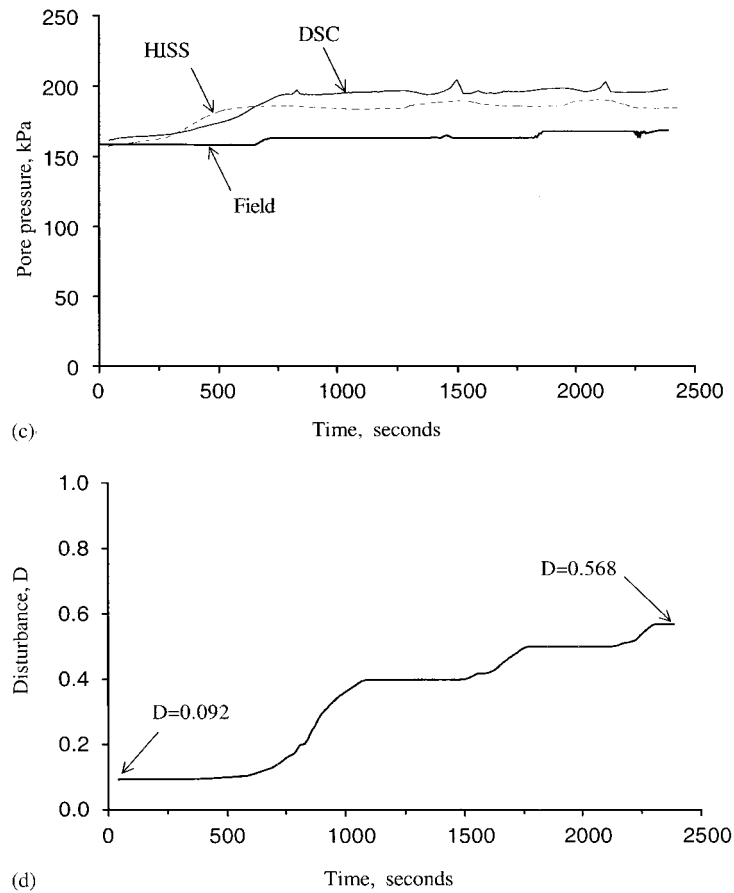


Figure 12. Continued.

the field measurements and prediction from HISS model in Figures 12(a)–12(c). Shear transfer from the current analysis with the DSC model is calculated by accumulating the induced vertical forces at the nodes with the prescribed displacements. While predicted shear transfer from the HISS model is lower than that from the field measurements, DSC yields much closer prediction of the shear transfer to the field data. The degradation of the peak value of the shear stress is also predicted well by the DSC. The proposed unloading and reloading model gives greater strain during the unloading, but the shapes of the reloading and unloading loop are predicted well. Predicted pore pressures, Figure 12(c), show an initial increase and then stable pore pressures which are higher than those from the field data.

Figure 12d shows the disturbance developed in element 121 in the one-way cyclic load test. Disturbance grows from 0.092 at the first time step to 0.568 after the final step. Though the value of disturbance in the thin-layer element (element 121) reached to 0.568, it was found that the disturbance in the elements beyond in the clay does not change significantly.

Simulation of final two-way cyclic load tests

Five field cycles in compression and tension to failure were performed for the 7.62 cm pile segment. The vertical displacements as measured in the field are applied to the nodes in contact with the pile segment (from E to F in Figure 10) in 801 time steps. Results from the finite element simulation are compared with field measurements and predictions from HISS model in Figure 13. Predicted values of shear transfer vs pile displacements are compared in Figure 13(a). The DSC prediction shows good agreement with the field behaviour and improvement over the HISS prediction. The DSC also predicts degradation between cycles, but within a given cycle the predicted degradation (softening) is not significant as in the field measurement. Proposed

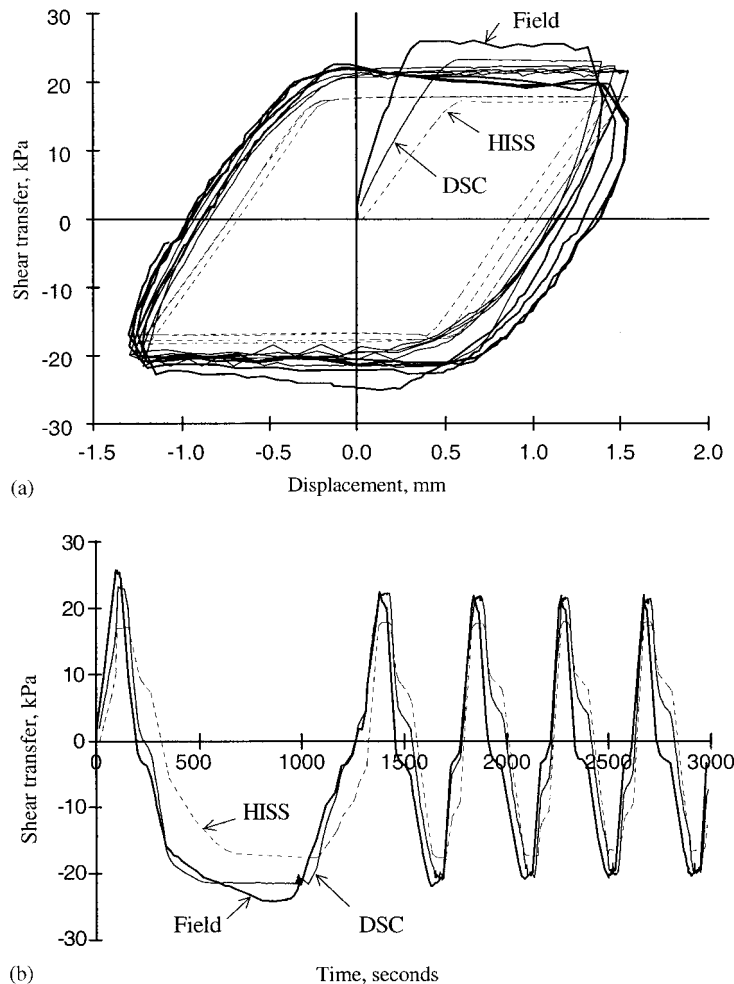


Figure 13. Comparison between field measurements and predictions from DSC and HISS models: two-way cyclic load test: (a) shear transfer vs displacement, (b) shear transfer vs time, (c) pore pressure vs displacement and (d) disturbance vs displacement.

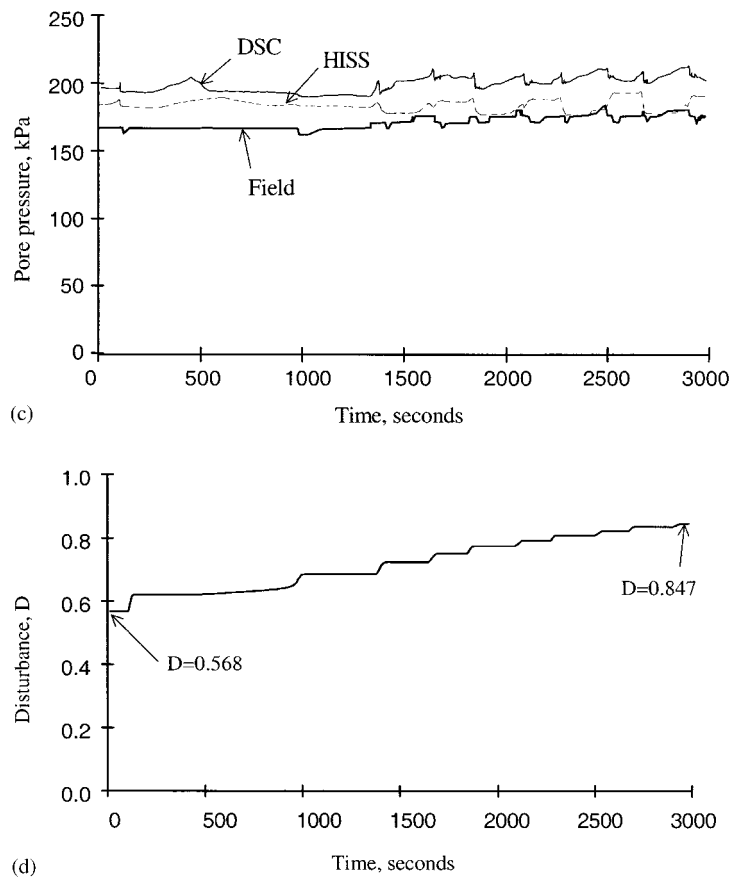


Figure 13. Continued.

unloading and reloading schemes perform well in this analysis. Figure 13b shows the predicted variation of shear transfer with time; it compares well with field measurements and shows improvement over the HISS model. Figure 13(c) compares the predicted variation of pore pressure vs time field measurements. The predicted values are higher than the measured values, but the trend agrees with the field measurements. The disturbance in element 121 changed from 0.568 to 0.847 as shown in Figure 13(d).

SUMMARY

The disturbed state concepts model was implemented in a non-linear finite element program for porous media. New and simplified unloading and reloading schemes were proposed and related formulation were developed and implemented. The parameters of the virgin and nonvirgin loading have clear physical meanings and are easy to find. The DSC model provides satisfactory correlation with laboratory stress-strain data for soils and interfaces.

Consolidation and cyclic loading tests of a field instrumented pile were numerically simulated using the finite element program and compared with field measurements and those from the previous analysis with the HISS model. The static and cyclic load analysis by using the DSC model provided good predictions of shear transfer from which the pile capacity can be evaluated; here also, the DSC model provides better prediction of the field tests than HISS plasticity model. The unloading and reloading procedure worked well in this analysis.

In general, the DSC model gives improved predictions of the field pile test over the HISS plasticity model. This is because the DSC allows for microstructural changes leading to degradation or softening, and interface motions are allowed in the present study. The finite element program with the DSC model can be used to solve static, consolidation and dynamic soil–structure interaction in dry or saturated conditions.

ACKNOWLEDGMENTS

The research results here were supported by grants Nos. CSM 9115316 and CES 8711764 from National Science Foundation (NSF), Washington, D.C.. The field pile load tests in the marine clay were performed by Earth Technology Corporation, Long Beach, California. Assistance of Prof. H. Matlock, G. Audibert, D. Bogard, P. Lam and L. Cheang is gratefully acknowledged.

REFERENCES

1. Desai CS. Constitutive modeling using the disturbed state concept as microstructure self-adjustment concept. In *Continuum Models for Materials with Microstructure*, Muhlhaus HB (ed.), Chapter 8. Wiley: U.K., 1995.
2. Desai CS, Ma Y. Modeling of joints and interfaces using the disturbed state concept. *International Journal for Numerical and Analytical Methods in Geomechanics*, 1992; **16**:623–653.
3. Armaleh SH, Desai CS. Modeling and testing of cohesionless material using disturbed state concept. *Journal of the Mechanical Behavior of Materials*, 1994; **5**:279–295.
4. Katti DR, Desai CS. Modeling and testing of cohesive soils using the disturbed state concept. *Journal of Engineering Mechanics ASCE* 1995; **121**:648–658.
5. Desai CS, Rigby DB. Cyclic interface and joint shear device including pore pressure effects. *Journal of Geotechnical and Geoenvironmental Engineering*, 1997; **123**:568–579.
6. The Earth Technology Corporation. Pile segment tests-sabine pass. *ETC Report No. 85-007*, The Earth Technology Corporation, Long Beach, California, 1986.
7. Desai CS. A consistent finite element technique for work-softening behavior. In *Proceedings of International Conference on Computational Method in Nonlinear Mechanics*, Oden JT (eds). Univ. of Texas: Austin, 1974.
8. Desai CS, Somasundaram S, Frantziskonis G. A hierarchical approach for constitutive modeling of geologic materials. *International Journal for Numerical and Analytical Methods in Geomechanics*, 1986; **10**:225–257.
9. Wathugala GW, Desai CS. Constitutive model for cyclic behavior of clays. 1. theory. *Journal of Geotechnical Engineering ASCE*, 1993; **119**:714–729.
10. Schofield AN, Wroth CP. *Critical State Soil Mechanics*. McGraw-Hill Book Company: London, 1968.
11. Shao C. Implementation of DSC model for dynamic analysis of soil–structure interaction problems. *Ph.D. Dissertation*, University of Arizona, Tucson, Arizona, 1998.
12. Dafalias YF, Hermann LR. Bounding surface plasticity II: application to isotropic cohesive soils. *Journal of Engineering Mechanics ASCE*, 1986; **112**:1263–1291.
13. Mroz Z. On the description of anisotropic work hardening. *Journal of Mechanics and Physics of Solids* 1967; **15**:163–175.
14. Iwan WD. On a class of models for the yielding behavior of continuous and composite systems. *Journal of Applied Mechanics Transactions ASME*, 1967; **34**(E3):612–617.
15. Prevost JH. Plasticity theory for soil stress–strain behavior. *Journal of Engineering Mechanics Division ASCE*, 1978; **104**(EM5):1177–1194.
16. Wathugala GW, Desai CS. Finite element dynamic analysis of nonlinear porous media with application to piles in saturated clays. *Report to NSF*, Dept. of Civil Engineering, University of Arizona, Tucson, Arizona, 1990.

17. Desai CS, Zaman MM, Lightner JG, Siriwardane HJ. Thin-layer element for interfaces and joints. *International Journal for Numerical and Analytical Method in Geomechanics*, 1984; **8**:19–43.
18. Biot MA. General solutions of the equations of elasticity and consolidation for a porous material. *Journal of Applied Mechanics*, 1956; **23**:91–96.
19. Zienkiewicz OC. Basic formulation of static and dynamic behavior of soil and other porous media. *Numerical Methods in Geomechanics*, Martins JB (ed.). D. Reidel Pub.: Dordrecht, 1981; 3–39.
20. Desai CS, Galagoda HM. Earthquake analysis with generalized plasticity model for saturated soils. *Earthquake Engineering and Structural Dynamics*, 1989; **18**:903–919.
21. Potts DM, Gens A. A critical assessment of methods of correcting for drift from the yield surface in elasto-plastic finite element analysis. *International Journal for Numerical and Analytical Methods in Geomechanics*, 1985; **9**:149–161.
22. Baligh MM. Undrained deep penetration, I: shear stresses. *Geotechnique*, 1986; **36**:471–485.
23. Baligh MM. Undrained deep penetration, II: pore pressures. *Geotechnique*, 1986; **36**:487–501.